

Slingshot Mechanism for Clusters: Gas Density Regulates Star Density in the Orion Nebula Cluster (M42)

Amelia M. Stutz^{1,2*}

¹*Departamento de Astronomía, Universidad de Concepción, Casilla 160-C, Concepción, Chile*

²*Max-Planck-Institute for Astronomy, Königstuhl 17, 69117 Heidelberg, Germany*

Accepted XXX. Received YYY; in original form ZZZ

ABSTRACT

We characterize the stellar and gas volume density, potential, and gravitational field profiles in the central ~ 0.5 pc of the Orion Nebula Cluster (ONC), the nearest embedded star cluster (or rather, proto-cluster) hosting massive star formation available for detailed observational scrutiny. We find that the stellar volume density is well characterized by a Plummer profile $\rho_{stars}(r) = 5755 M_{\odot} \text{pc}^{-3} (1 + (r/a)^2)^{-5/2}$, where $a = 0.36$ pc. The gas density follows a cylindrical power law $\rho_{gas}(R) = 25.9 M_{\odot}/\text{pc}^3 (R/\text{pc})^{-1.775}$. The stellar density profile dominates over the gas density profile inside $r \sim 1$ pc. The gravitational field is gas-dominated at all radii, but the contribution to the total field by the stars is nearly equal to that of the gas at $r \sim a$. This fact alone demonstrates that the proto-cluster cannot be considered a gas-free system or a virialized system dominated by its own gravity. The stellar proto-cluster core is dynamically young, with an age of ~ 2 -3 Myr, a 1D velocity dispersion of $\sigma_{\text{obs}} = 2.6 \text{ km s}^{-1}$, and a crossing time of ~ 0.55 Myr. This timescale is almost identical to the gas filament oscillation timescale estimated recently by Stutz & Gould (2016). This provides strong evidence that the proto-cluster structure is regulated by the gas filament. The proto-cluster structure may be set by tidal forces due to the oscillating filamentary gas potential. Such forces could naturally suppress low density stellar structures on scales $\gtrsim a$. The analysis presented here leads to a new suggestion that clusters form by an analog of the "slingshot mechanism" previously proposed for stars.

Key words: open clusters and associations: individual: M42 (ONC) - Stars: formation - Infrared: stars - ISM: clouds - Clouds: Individual: Orion A

1 INTRODUCTION

The Orion Nebula Cluster (ONC, also known as M42) is the nearest site of massive star formation and significant embedded cluster available for detailed observational scrutiny. At a distance of ~ 400 pc (e.g., Menten et al. 2007; Sandstrom et al. 2007; Schlafly et al. 2014; Kounkel et al. 2017) it has been the subject of many studies (e.g., Jones & Walker 1988; Hillenbrand & Hartmann 1998; Kroupa et al. 1999; Kroupa 2000; Kroupa et al. 2001; Hartmann & Burkert 2007; Tobin et al. 2009; Megeath et al. 2012, 2016; Meingast et al. 2016; Da Rio et al. 2016; Portegies Zwart 2016) scrutinizing in detail the stellar and protostellar content of the region. Generally, these studies have restricted themselves to the investigation of the stellar content of the cluster for lack of high quality observations that reliably trace the total gas

mass distribution, which have only been obtained recently (Stutz & Kainulainen 2015; Stutz & Gould 2016).

The ONC is directly associated with a larger high line-mass gas filament called the Integral Shaped Filament (ISF; Bally et al. 1987; Tatematsu et al. 2008; Stutz & Gould 2016; Kainulainen et al. 2016). The ONC is partially embedded in the high density filament and lies slightly in foreground (e.g., O'dell 2001; Wen & O'dell 1995), as is apparent from the continuous distribution of stellar extinctions (S. T. Megeath, private communication 2017). The filament, with a wave-like morphology, has dimensions of ~ 7.3 pc in height and a horizontal oscillation semi-amplitude of ~ 1.5 pc (Stutz & Gould 2016). The stellar distribution is highly elongated as the stars follow the gas (e.g., Hillenbrand & Hartmann 1998; Da Rio et al. 2014; Megeath et al. 2016; Stutz & Kainulainen 2015; Stutz & Gould 2016). Indeed, significant effort has been dedicated to characterizing the asymmetries in the projected stellar distribution (e.g., Megeath et al. 2016, and references above). Nevertheless, the relationship

* E-mail: astutz@astro-udec.cl, stutz@mpia.de

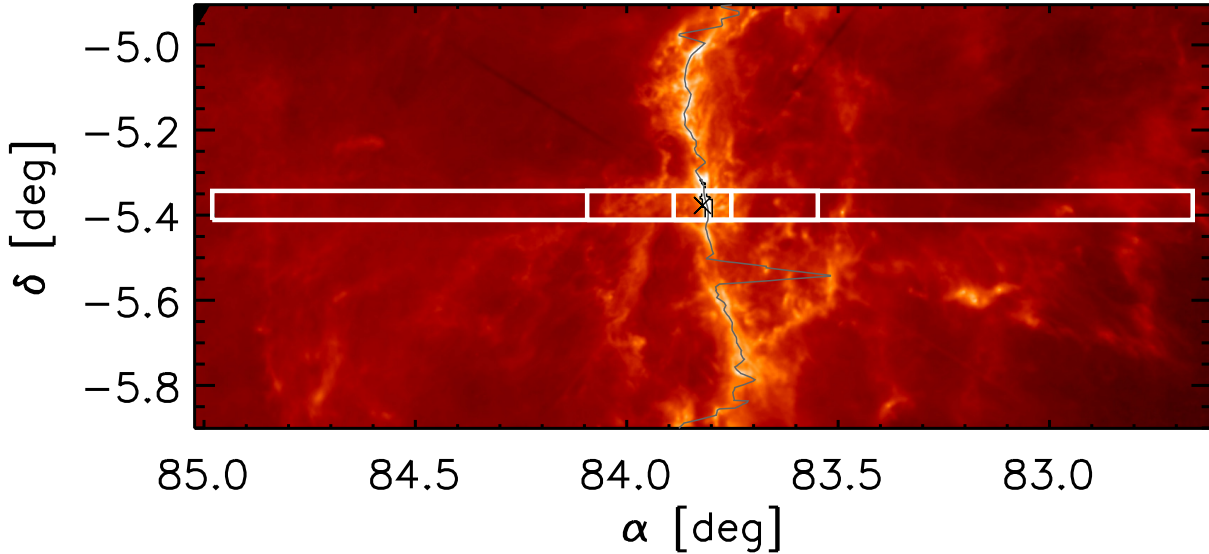


Figure 1. $N(\text{H})$ map from [Stutz & Kainulainen \(2015\)](#) of the Integral Shaped Filament (ISF, including M42). The vertical scale of the figure is 7.3 pc, the horizontal scale is ~ 17 pc. The saturated map region within which we apply the APEX $870\mu\text{m}$ correction is indicated by the black contour (see text for details). The grey line shows the dust ridgeline ([Stutz & Gould 2016](#)). The \times -symbol indicates the stellar center of mass of the ONC. The large white box is $0.5\text{ pc} \times 17\text{ pc}$ in size while the inner vertical lines indicate radii of 0.5 pc and 2.0 pc.

between the stellar and gas volume density structures in the central ~ 0.5 pc of the ONC has so far remained unexplored.

Recently, [Stutz & Gould \(2016\)](#) proposed, based on a high density of observations, that the gas filament in the ISF is oscillating and ejecting young stars (the “Slingshot”, see also [Boekholt et al. 2017](#); [Schleicher & Stutz 2017](#)). Given the extremely close association of the ONC stars with the gas filament, this scenario immediately raises the question of whether such filamentary gas oscillations might affect the structure of the embedded stellar cluster. Here we investigate this possibility through analysis of both the stellar ([Megeath et al. 2016](#)) and gas ([Stutz & Kainulainen 2015](#); [Stutz & Gould 2016](#)) distributions in the center of the ONC.

Previous efforts at simulating open cluster formation have focused mainly on proto-cluster formation within turbulent molecular clouds (e.g., [Bate 2009](#); [Fujii & Portegies Zwart 2016](#)). Here, proto-clusters (or embedded clusters) are distinct entities from clusters. Both are defined by concentrations of stars whose gravity is sufficiently strong to influence the stellar dynamics. However, in clusters, the gravity is dominated by the stars whereas in proto-clusters it is dominated by the gas out of which the stars are still forming. With this analysis we provide the essential ingredients necessary for simulating cluster formation conditions in ONC-analogs, in which clusters form on massive dynamical gas filaments. We quantify both the stellar and gas volume density distributions using simple geometric assumptions and discuss the relationship between them. We find that the gas and star gravitational field profiles reach near-equality at $r = a = 0.36\text{ pc}$, the softening scale of the stellar density profile. At all other radii the gas dominates the gravitational field. This, combined with the fact that the cluster crossing time is very similar to the estimated timescale for the gas filament motions, strongly suggests that the cluster profile and dynamics are controlled by the gas filament.

2 GAS AND STELLAR MASS MAPS

2.1 Gas mass map

We use the column density map from [Stutz & Kainulainen \(2015\)](#); see also [Stutz & Gould 2016](#)). This map was derived from the *Herschel* dust emission data at $160\mu\text{m}$, $250\mu\text{m}$, $350\mu\text{m}$, and $500\mu\text{m}$. The final resolution of the map is about $20''$. We refer the reader to [Stutz & Kainulainen \(2015\)](#) for further details.

The [Stutz & Kainulainen \(2015\)](#) $N(\text{H})$ map was corrupted due to saturation in the center of the Orion Nebula Cluster (ONC) over a small elongated region covering less than $1.5' \times 6'$. We correct this defect using the APEX $870\mu\text{m}$ data (e.g., [Stanke et al. 2010](#); [Stutz et al. 2013](#)). This correction assumes that: (1) the spatial filtering in the ground-based submillimeter data is negligible across the narrow extent of the *Herschel* $N(\text{H})$ map artifact (with a maximum width of $\sim 1.5'$); and (2) the $870\mu\text{m}$ emission is optically thin and traces the same dust emission as the *Herschel* maps. We use the region immediately outside the saturation artifact to scale the $870\mu\text{m}$ data in E-W strips to fill in the missing column density information.

Figure 1 shows the corrected $N(\text{H})$ map of the Integral Shaped Filament (ISF) region, with M42 and the forming star cluster (ONC) located in the center. The grey line in Figure 1 is our recalculated dust ridgeline (for details see [Stutz & Gould 2016](#)) based on the corrected $N(\text{H})$ maps, which follows the maximum $N(\text{H})$ as a function of δ . It is interesting to note the spike in the dust ridgeline near $\delta = -5.5^\circ$, caused by discontinuity in the filament that causes the ridgeline to “jump” to the to the nearest $N(\text{H})$ maximum, in this case to the west of the main filament. The filament also appears discontinuous in the high density gas tracer N_2H^+ ([Tatematsu et al. 2008](#); [Hacar et al. 2017](#)), indicating that while the filament appears approximately like

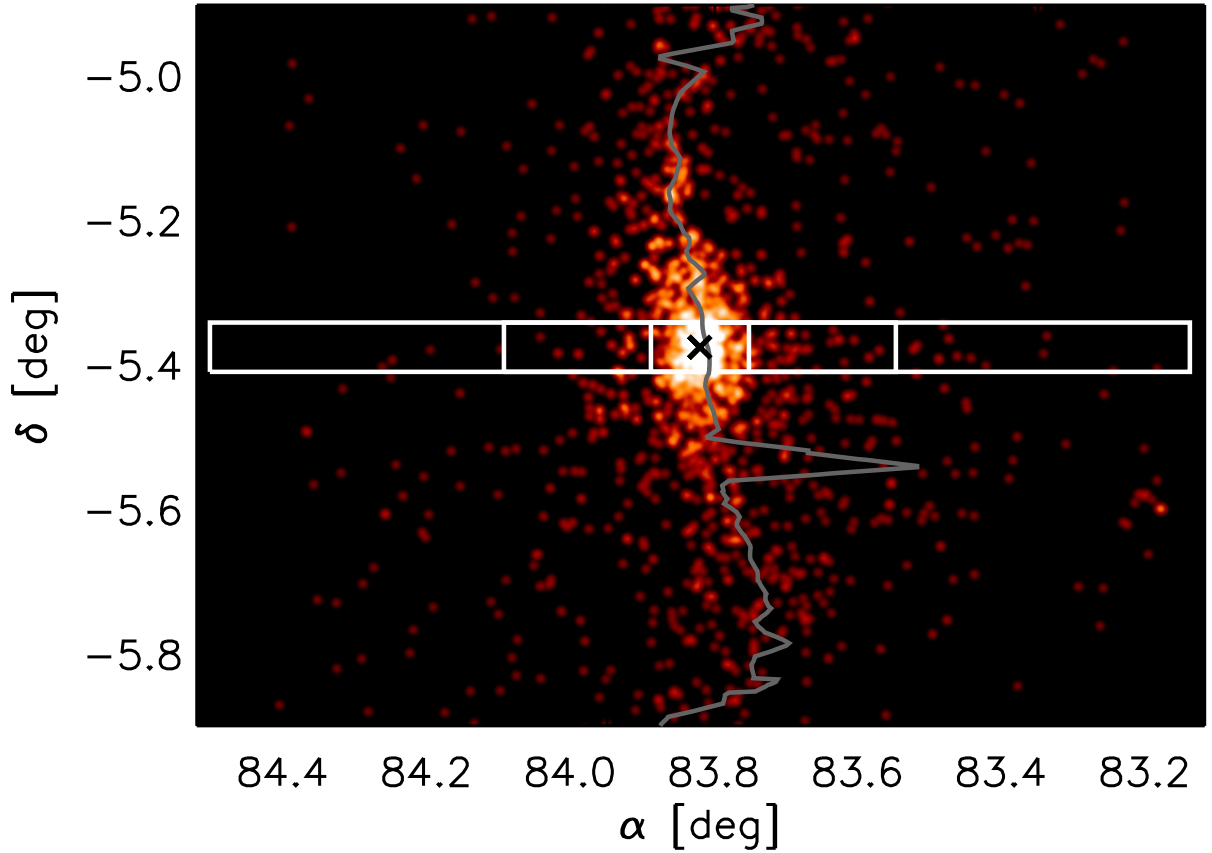


Figure 2. Star mass map of the ISF. The vertical scale of the figure is 7.3 pc, the horizontal scale is ~ 10 pc. The \times -symbol indicates the stellar center of mass of the ONC at $\alpha = 05:35:17.0$, $\delta = -05:22:37.95$. The dust ridgeline is indicated as a dark-grey line. The white box is $0.5 \text{ pc} \times 10 \text{ pc}$ in size. The large white box is $0.5 \text{ pc} \times 10 \text{ pc}$ in size while the inner vertical lines indicate radii of 0.5 pc and 2.0 pc .

a single structure, it is in fact being broken apart at this location immediately below the cluster formation site (see discussion).

2.2 Stellar mass map

We use the disk star count map of Orion A based on the *Spitzer* data analyzed in detail by Megeath et al. (2016) (see also Megeath et al. 2012). Figure 2 shows the stellar mass map. Briefly, in our map each young star is represented by a delta function and then convolved to a $37''$ beam size (approximately matching the *Herschel* $500 \mu\text{m}$ beam). The weight of each delta function is equal to the inverse estimated local incompleteness at the source location. In regions of high nebulosity such as the center of the ONC the completeness correction fails due to the limited amount of information in the images. Therefore Megeath et al. (2016) use the COUP x-ray data (Feigelson et al. 2005) to augment the incomplete *Spitzer* counts. To accomplish this, Megeath et al. (2016) apply weighting factors to account for two principal effects:

1. The COUP data detect a different source population

than the *Spitzer* data: *Spitzer* is based on IR excess, while the COUP data are sensitive to all x-ray emitting stars.

2. The *Spitzer* data are incomplete due to nebulosity (see above).

In order to account for these effects and match the two datasets, Megeath et al. (2016) compare the nebulosity-corrected *Spitzer* counts to the COUP surface densities in the region of overlap where both the *Spitzer* and COUP incompleteness are minimized (that is, outside of the core of the ONC) to scale the COUP profile to the *Spitzer* counts. In the regions where the *Spitzer* data do not provide complete information, the scaled COUP counts are used. This analysis is described in detail in Megeath et al. (2016). The total number of stars with disks across Orion A is 5265. The total number of stars with disks in the ISF (shown in Fig. 2) is 3344, while the total number of stars within the box centered on the ONC (see Fig. 2) is 1031. The *Spitzer* and COUP counts can in principle also be used without a nebulosity correction, and the resulting mass distribution differences are discussed below.

To convert the young star count map into a total stellar mass map we must assume two quantities: 1.) a mean stellar mass of $0.5 M_{\odot}$ (Kroupa et al. 2001), and 2.) a disk fraction

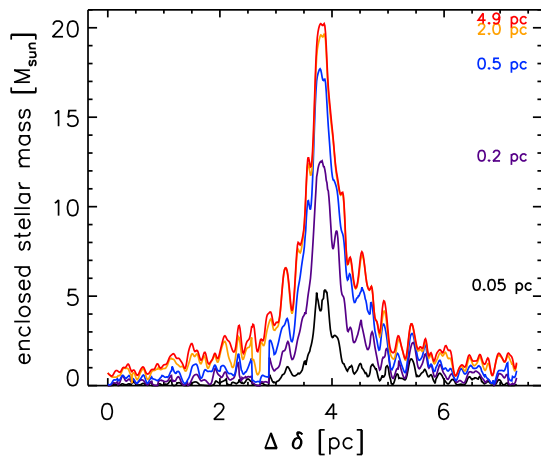


Figure 3. Enclosed stellar mass at a given declination starting from the Southern edge of ISF (at Dec. = -5.9°) to the northern edge (Dec. = -4.9°). Different curves indicate the mass enclosed within various projected radii from the dust ridgeline. The maximum extent of the stellar mass distribution is about 5 pc although most of the stellar mass lies within 2 pc of projected distance from the dust ridgeline.

of 0.75 (Megeath et al. 2016). Figure 2 shows the projected stellar mass distribution of the ISF. Ideally, we would base the conversion from star counts to stellar mass on empirically observed quantities, such as direct measurements of the IMF. Da Rio et al. (2012) measure the ONC IMF over a region covering about $30' \times 30'$. Based on various evolutionary tracks they measure the (model dependent) characteristic mass (the peak IMF mass) to be about $0.3 M_\odot$ (see their Table 4). As they note, this relatively high characteristic value is driven by their finding that the low mass population is deficient compared to other regions. They argue that incompleteness at low masses is not driving this result. Such values would correspond to somewhat higher mean stellar masses than those assumed here. Nevertheless, given the status of the current observational evidence, our assumed mean stellar mass is justified. Furthermore, our basic ONC results are not affected by small shifts in the assumed mean stellar mass as these will not change the shape of the fitted density profile (see below). Our disk fraction assumption of 0.75 is analyzed in detail in Megeath et al. (2016). We refer the reader to that work (specifically Sect. 2.2) for discussion on the derivation of the disk fraction. We note that Getman et al. (2014) argue for a higher disk fraction in the center of the ONC. However, small shifts in this number do not affect our results (see below). Here we follow Megeath et al. (2016) and assume a single average disk fraction throughout our map. This approach works well in regions dominated by disk stars, such as the ONC.

3 STELLAR MASS DISTRIBUTION OF THE ISF

We begin by analyzing the stellar mass distribution as a function of δ and projected radial distance (w) from the gas

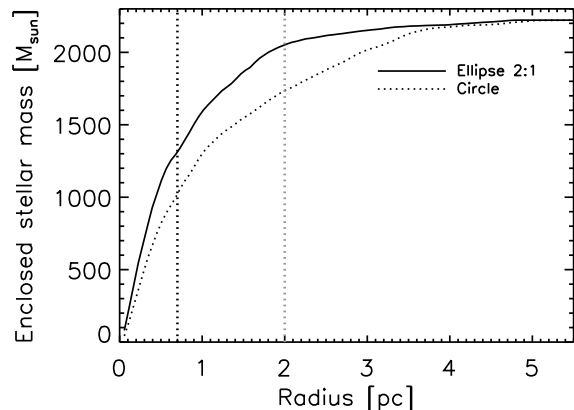


Figure 4. Stellar mass inside projected radii for elliptical (solid line, 2:1 axis ratio with long axis oriented North-South) and circular apertures (dotted line). Here the “radius” of the ellipse corresponds to the minor axis of the elliptical aperture. Vertical dashed lines indicate the extent of the main structural components of the ONC: a clear stellar cluster core with $r \sim 0.7$ pc and a more extended but lower density “halo” extending to about $r \sim 2.0$ pc. The total stellar mass associated with the ISF is about $2200 M_\odot$. The cluster mass within $r \sim 0.7, 2.0$ pc is about 1300, $2000 M_\odot$.

ridgeline in Figure 3. The highly non-uniform stellar mass distribution is evident, and peaks approximately in the center of the ISF at the location of the ONC. Furthermore, the vast majority of the stellar mass is located within a projected radial distance of about 2 pc from the dust ridgeline, consistent with the Stutz & Gould (2016) measurement of $\langle r_\perp \rangle = 1.48$ pc for the disk stars with APOGEE radial velocity measurements.

By analyzing the stellar mass profiles as a function of w , centered on the peak of the stellar mass distribution located at $\alpha = 05:35:16.49$, $\delta = -05:22:54.73$ we obtain a measurement of the projected cluster structure. Figure 4 shows that the stellar mass distribution can be separated into three regions, separated at $w \simeq 0.7, 2.0$ pc. Based on the above figures we conclude that:

1. The star cluster “core” at the center of the ISF has a projected radius $\lesssim 0.7$ pc, corresponding to the rich center of the ONC where it is difficult to differentiate between a spherical symmetry and an elongated (elliptical) structure.
2. The star cluster “core” has minimal departures from circular symmetry below a projected radius $\lesssim 0.5$ pc.
3. The ONC has a mass of ~ 1000 to $1300 M_\odot$ within a radius of 0.7 pc.
3. The total stellar mass in the ISF is $\sim 2200 M_\odot$.
4. There are $\sim 900 M_\odot$ of stars outside $r = 0.7$ pc, distributed in a lower density stellar “halo”.
5. These “halo stars” have a distribution that surrounds the main central cluster, but follows the gas filament (i.e., is highly elongated).

In particular, we emphasize that in the center of the cluster, at radii $\lesssim 0.5$ pc, Figure 4 shows that the departures from circular symmetry are minimal. That is, the differences between the elliptical and circular apertures in the cumula-

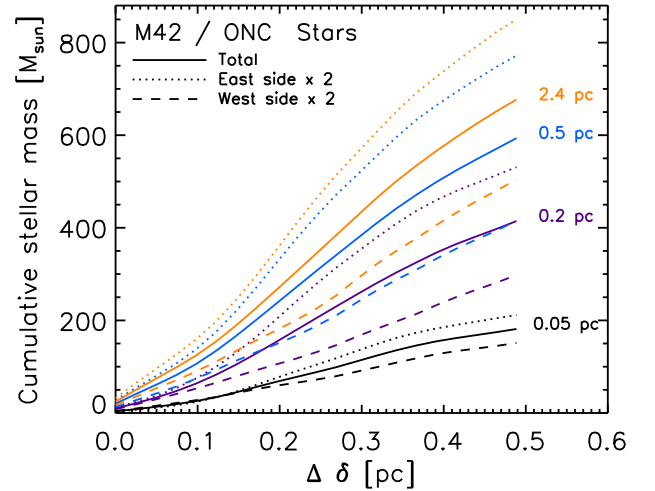
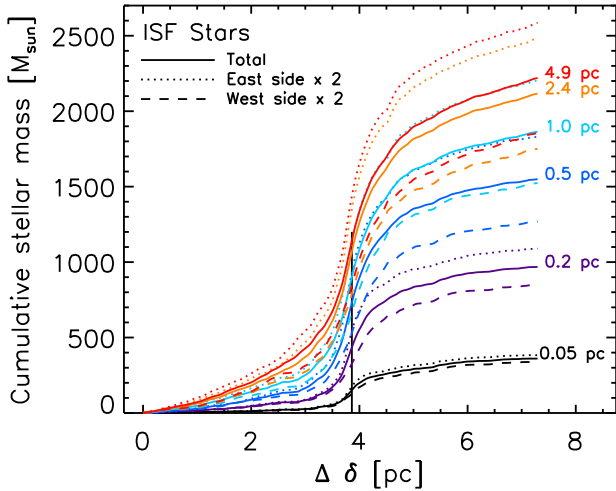
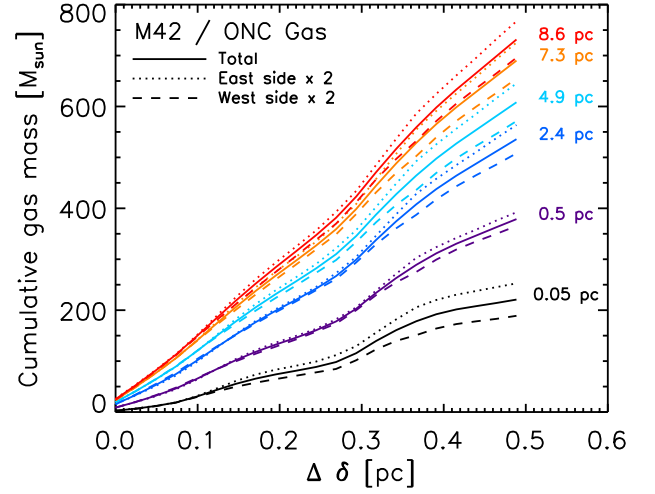
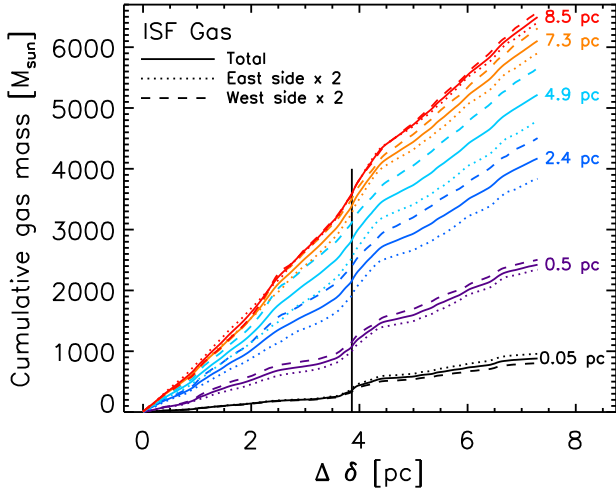


Figure 5. Cumulative distributions of gas (*top*) and stellar (*bottom*) mass within various projected separations w from the dust column density ridgeline for the ISF. The cumulative distributions start at the southern boundary of the ISF ($\text{Dec} = -5.9^\circ$). The separate cumulative distributions for the east ($-w < x < 0$) and west ($0 < x < +w$) are shown in different line types. For ease of comparison (and clarity) these are multiplied by two. The vertical black line indicates the δ of the stellar center of the ONC.

Figure 6. Same as Figure 5 zoomed in on the central 0.5 pc of the ONC.

tive mass profiles are small, reaching 27% at $r = 0.5$ pc. These differences are small compared to the overall variations in the density profile (see below). Thus the assumption of spherical symmetry is reasonable.

4 ONC GAS AND STAR VOLUME DENSITY, GRAVITATIONAL POTENTIAL, AND GRAVITATIONAL FIELD

It is clear from Figure 5 that the gas (top panel) and stellar mass (bottom panel) distributions are radically different. The ISF stars exhibit a large mass concentration in the center of the gas filament in the ONC (e.g., Megeath et al.

2016). This stands in contrast to the gas mass distribution, which is very close to uniform along the ISF, as Stutz & Gould (2016) showed. In addition, this figure shows that the correction to the saturated portion of the Herschel N(H) image has a negligible effect on the gas mass distribution profiles of the ISF (see Figure 4 of Stutz & Gould 2016 for the ISF mass distributions without the APEX 870 μm correction). We note that previous works have characterized the projected stellar surface density distributions of the ONC (Megeath et al. 2016, ; see also Gutermuth et al. 2015, 2009 for methodology) and show that the stellar distribution has departures from circular symmetry on scales $\gtrsim 0.5$ pc. Here we adopt the approximation of spherical symmetry in the case of the stars in order to execute a simple volume density analysis. This assumption is valid on small scales near the stellar cluster core, and not on larger scales as has been previously shown (see above references). Thus, Figures 4 and 5 motivate scrutinizing a narrow range in δ within which

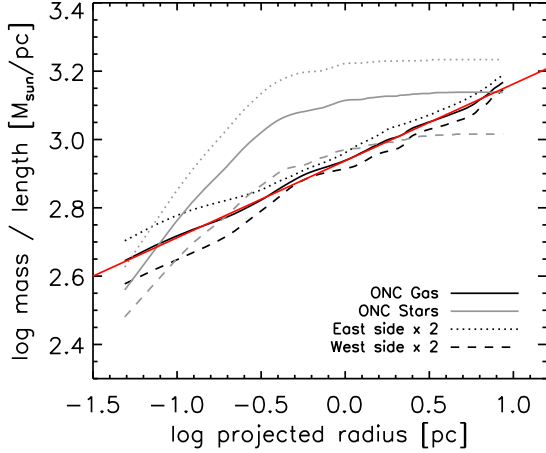


Figure 7. Cumulative mass/length as a function of enclosing width w integrated over a width in $\delta=0.5$ pc centered on the ONC. The ONC gas (black) and stars (grey) are shown separately. As in Figure 6, the east and west subsets are shown separately (after multiplying by 2). The red line indicates a power law of slope $\gamma=0.225$ (see eqn. 1).

the stellar mass distribution is far more concentrated and a circular (or spherical) approximation is reasonable.

To this end we analyze the cumulative gas and stellar mass distributions centered on the ONC star cluster, shown in Figure 6. Here we analyze a much smaller range in δ of 0.5 pc, indicated with boxes in Figures 1 and 2. Both the gas and star mass distributions are calculated relative to the dust ridgeline (see above and Stutz & Gould 2016). The top panel of Figure 6 shows the gas mass distribution over the center of the ONC, while the bottom panel shows the stellar mass distribution. From this figure we can see that the cumulative gas mass increases relatively smoothly across the 0.5 pc extent of the ONC region that we are scrutinizing, although not as smoothly as for the ISF as whole (see Figure 5 and Stutz & Gould 2016). Meanwhile, the stellar mass distribution exhibits significant curvature associated with underlying circular (or spherical) structure of the cluster.

Taking advantage of the simple geometry implied by the two distributions (cylindrical for gas and spherical for stars) we construct mass per unit length profiles for both, shown in Figure 7. Here, the projected mass per unit length (M/L) profiles are integrated over a height $\delta = 0.5$ pc centered on the region of highest projected stellar density, the center of the ONC. In practice this represents the M/L profile over a thin “orange slice” centered on the equatorial plane of the stellar cluster. This thin slice approach allows us to analyze the gas and star distributions in the direction perpendicular to the gas filament using simple geometric considerations. In particular, this approach allows us to ignore the more complex geometry of the star distribution on larger scales, where elongation along the gas filament precludes an accurate analysis using spherical or azimuthal averaging.

4.1 ONC Gas

Assuming cylindrical geometry, the gas distribution follows a power law of the form

$$\lambda(w) = K \left(\frac{w}{\text{pc}} \right)^\gamma; \quad K = 866 \frac{M_\odot}{\text{pc}}, \quad \gamma = 0.225. \quad (1)$$

Here w is the projected radius as observed on the plane of the sky (or the impact parameter to the dust ridgeline). This power law has a different normalization and index than that of the ISF filament as a whole¹ (Stutz & Gould 2016). We discuss this difference below. Such a power law line mass distribution can be easily converted to a gas volume density profile assuming cylindrical symmetry following Eqn. 5 of Stutz & Gould (2016):

$$\rho(R) = 25.9 \frac{M_\odot}{\text{pc}^3} \left(\frac{R}{\text{pc}} \right)^{\gamma-2}. \quad (2)$$

Following Stutz & Gould (2016) we also obtain the enclosed gas line density $\Lambda(R)$, acceleration $a(R)$, and the gravitational potential profiles:

$$\Lambda(R) = f(\gamma)\lambda(R) = 0.83\lambda(R) = 723 \frac{M_\odot}{\text{pc}} \left(\frac{R}{\text{pc}} \right)^\gamma, \quad (3)$$

$$a(R) = 2G\Lambda/r = 6.2 \text{ km s}^{-1} \text{ Myr}^{-1} \left(\frac{R}{\text{pc}} \right)^{\gamma-1}, \quad (4)$$

and

$$\Phi(R) = \eta(\gamma)G\Lambda(R) = 27.6 (\text{km s}^{-1})^2 \left(\frac{R}{\text{pc}} \right)^\gamma. \quad (5)$$

Here, $f(\gamma)$ and $\eta(\gamma)$ are defined in Stutz & Gould (2016), and have values of 0.834 and 7.418 respectively for $\gamma = 0.225$.

4.2 ONC stars

Assuming spherical symmetry in the stellar core, we determine the stellar volume density using a model of the form

$$\Sigma_s(b) \propto (1 + (b/a)^2)^{-\beta} \quad (6)$$

to analyze the projected stellar M/L profile (Fig. 7). This is a generalized form of the projected surface density of a Plummer profile; a value of $\beta = 2$ gives the familiar Plummer profile (Plummer 1911; Binney & Tremaine 2008), which has a well defined density-potential pair, and is commonly used to characterize star cluster profiles (e.g. Portegies Zwart et al. 2010; Bianchini et al. 2017). In Figure 8 we show various M/L curves for different values of both β and a . The best match to the observed stellar distribution is given by $\beta = 2$ and $a = 0.36$ pc. All models in Figure 8 are normalized at large radii ($r = 1$ pc with $M_{\text{slice}}/L = 1285 M_\odot/\text{pc}$, see below). The normalization at small radii then strongly discriminates against most models. No model fits the data perfectly. In particular, those that fit well at intermediate projected radii are slightly too low at very small projected radii. Two models appear to fit the data at intermediate radii, $(\beta, a) = (2.0, 0.36 \text{ pc})$ and $(\beta, a) = (2.5, 0.44 \text{ pc})$. Since

¹ Stutz & Gould (2016) measure values of $K = 385 M_\odot \text{ pc}^{-1}$ and $\gamma = 3/8$ (see their Eqn. 4) for the ISF as a whole.

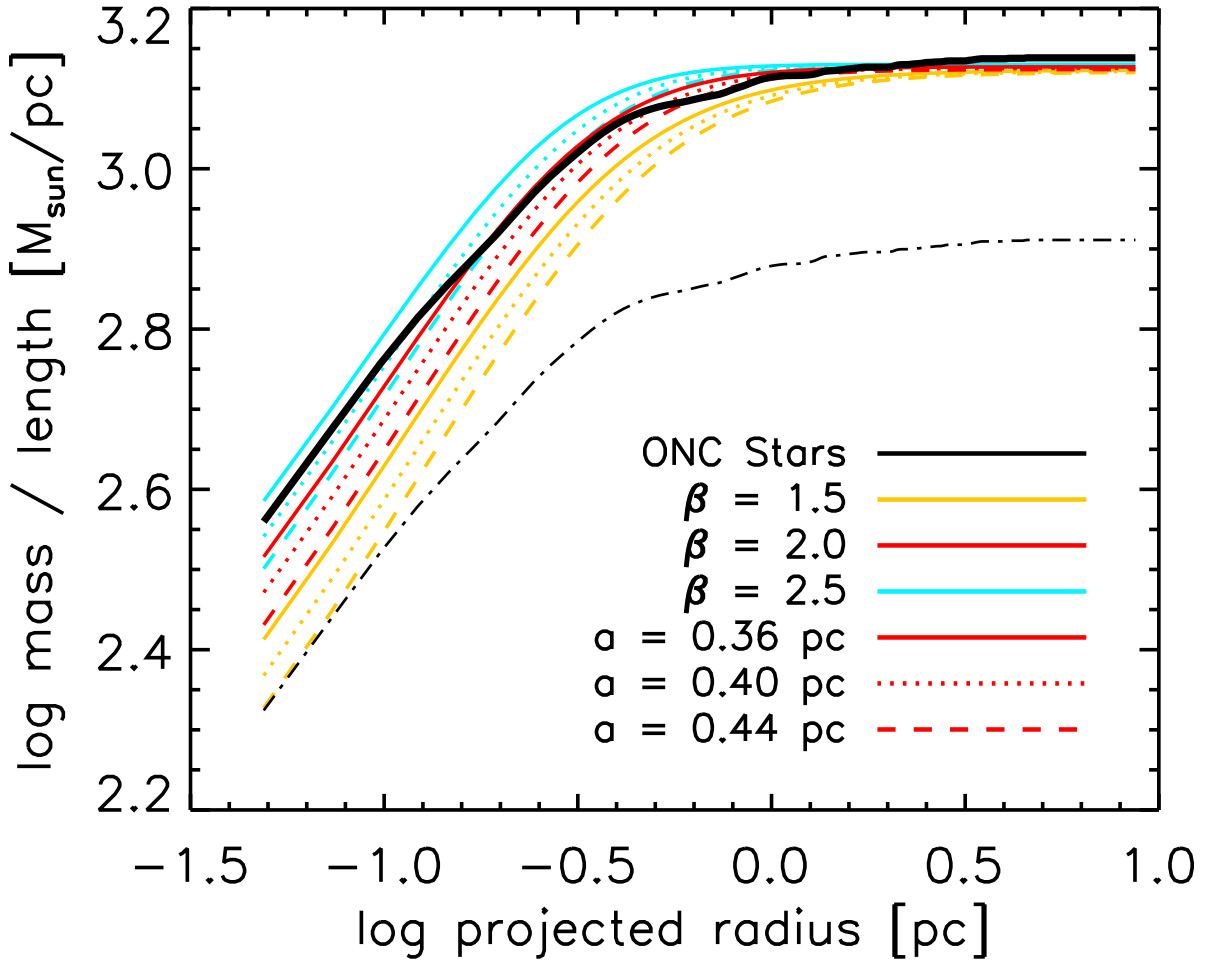


Figure 8. Model fits to the stellar mass distribution in Fig. 7 using equation 6. The best-fit model to the stellar distribution corresponds to the red-dashed line, that is, to $a = 0.36$ pc and $\beta = 2$ (i.e., a Plummer profile). Here we adopt $M_{\text{slice}}/L = 1285 M_{\odot}/\text{pc}$ at $r = 1$ pc as the total mass per unit length for the fit (see text). The dot-dashed line corresponds to the *Spitzer* star counts when ignoring the effects of nebulosity (see text and Megeath et al. 2016).

$(\beta, a) = (2.0, 0.36 \text{ pc})$ fits at the intermediate radii almost perfectly and is closer to the data at small radii, we adopt this model as a good analytic representation of the stellar profile.

From simple analytic analysis, we show in Appendix A that for the case of $\beta = 2$, we obtain a relation between M/L measured in a thin slice and the volume density profile, where

$$\rho_s(r) = K(1 + (r/a)^2)^{-\gamma}; \quad \gamma = \beta + 0.5, \quad (7)$$

and

$$K = \frac{3}{2\pi a^2} \frac{M_{\text{slice}}}{L} \sqrt{1 + (L/2a)^2}. \quad (8)$$

Here, $M_{\text{slice}}/L = 1285 M_{\odot}/\text{pc}$ is the value of the stellar M/L measured from Figure 8 at $r = 1$ pc.

The final volume density profile of the stars is

$$\rho_s(r) = 5755 \frac{M_{\odot}}{\text{pc}^3} (1 + (r/a)^2)^{-5/2}. \quad (9)$$

The corresponding gravitational acceleration and potential profiles are

$$a_s(r) = 37.3 \text{ km s}^{-1} \text{ Myr}^{-1} (1 + (r/a)^2)^{-3/2} r/a, \quad (10)$$

and

$$\Phi_s(r) = -13.4 (\text{km s}^{-1})^2 (1 + (r/a)^2)^{-1/2}. \quad (11)$$

The mass and density profiles are consistent with previous investigations into the density structure as a whole, for which e.g., Da Rio et al. (2014) find that a slope of $\gamma \sim 2.2$ for the volume density profile. In agreement with Hillenbrand & Hartmann (1998), we find an inner flattening of the core density profile. Below $r \sim 0.36$ pc the stellar surface

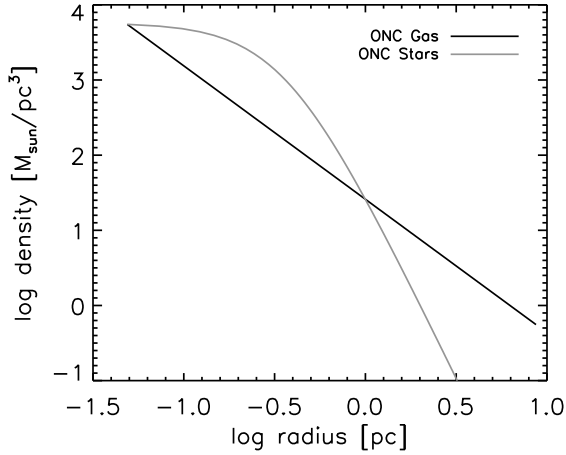


Figure 9. Volume density profiles of gas (black curve) and stars (grey) corresponding to the cumulative distributions shown in Figure 7.

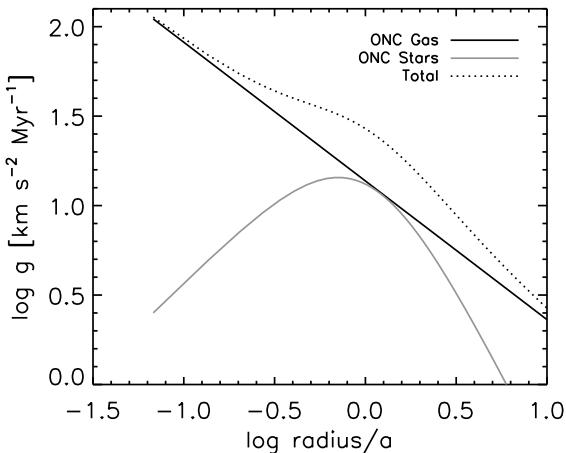


Figure 10. Gravitational field of gas (black curve) and stars (grey curve) corresponding to the density profiles shown in Figure 9. The gas and star profiles reach near-equality at $r = a = 0.36pc$, while the gravitational field due to the gas dominates everywhere else.

density flattens, and is inconsistent with a power-law distribution that would continue into the center of the cluster. In terms of the density profile, the values of β and a do not depend on the overall normalization of the M/L profile. For comparison to Megeath et al. (2016), in Figure 8 we show the M/L profile for the mass profile based on the maps neglecting the nebulosity correction (see Section 2). The shape of the M/L profile is the same, but the normalization is a factor of 1.7 lower, with a value of $M_{\text{slice}}/L = 746.7 M_{\odot}/pc$. Thus, the parameters for the shape of the volume density profile would not be affected. However, the nebulosity correction is essential for obtaining accurate stellar profiles. Therefore in what follows we use the fully corrected profiles.

5 DISCUSSION AND CONCLUSIONS

In Figure 9 we show the volume density profiles for the gas (black curve) and stars (grey curves). One of the most striking features of this diagram is that the stellar density surpasses the gas inside $r \sim 1 pc$, but outside the system is gas dominated. In Figure 10 we show the corresponding gravitational field profiles for the gas, stars, and total. The stars contribute a maximum to the field at $r/a \sim 0.8$ ($\sim 0.3 pc$), and have about equal contribution as the gas near $r/a \sim 1.1$ ($\sim 0.45 pc$). That is, the stars contribute most significantly to the field at $r \sim a$, while the gas dominates at all other radii, both smaller and larger.

We estimate the cluster crossing time $t_{\text{cross}} = 2a/\sigma_{\text{obs}} \sim 0.55 Myr$, where $a = 0.36 pc$ and $\sigma_{\text{obs}} = 2.6 km s^{-1}$. We measure a velocity dispersion for the stars of $\sigma_{\text{obs}} = 2.6 km s^{-1}$ from the APOGEE data (e.g., Stutz & Gould 2016; Da Rio et al. 2016). Then we must estimate the size of the cluster, i.e. the radius of a sphere containing the stars having a velocity $\sim 2.6 km s^{-1}$. This can be obtained from the data, for example from Figure 9 where we can estimate a characteristic radius (containing most of the stars) as $2a$. If the lifetime of the ONC is $\sim 2-3 Myr$ (Da Rio et al. 2016), then the core is about 4-6 crossing times young. On this relatively short timescale we do not expect significant internal evolution to have taken place in the cluster. Furthermore, Stutz & Gould (2016) estimate the timescales of the gas filament motion of $\sim 0.6 Myr$, which is very similar to the cluster t_{cross} .

The ensemble of evidence presented here strongly suggests that the cluster profile and dynamics are controlled by the gas filament. First, the gravitational field is everywhere dominated by the gas. This fact alone, established here for the first time, demonstrates that the stellar cluster cannot be considered a virialized system dominated by its own gravity. Second, the transition from cluster core to halo (at softening radius a) occurs at exactly the point that the cluster gravity would begin to dominate that of the gas. This indicates that the gas potential somehow limits the growth of the cluster core. That is, the structural parameters of the star cluster might be determined by the gas filament. Third, the internal cluster timescale is the same as the oscillation timescale of the filament, which is measured on spatial scales that are an order of magnitude larger than the cluster.

The coincidence of timescales, together with the fact that the filament oscillations are clearly independent of the cluster, implies that it is these oscillations that are driving the internal dynamics of the cluster. The driver for the gas oscillations is rooted in the interaction between the magnetic field and gravity of the gas filament. That is, the magnetic field is not felt by the stars, they move independently, only affected by gravity, both their own and that of the gas. Yet the gas does feel the magnetic field. The gas is distributed in a $\sim 7 pc$ long filament which is much larger and more massive than the star cluster, and which has a wave-like morphology (and kinematics) that indicates that the gas is oscillating, as proposed by Stutz & Gould (2016). In this picture, the gas oscillations are determined by the interaction of the magnetic field and the gravitational potential of the gas (which completely dominates over the potential of the stars, except in a small region near $r = a$ in the center of the ONC). The gas then has a causal relationship to

the stellar cluster, whereby the gas oscillations imprint on the stellar cluster structure through changes in the gravitational field (felt by the cluster) which are caused by the accelerating gas filament. To second order, the density enhancement of the stars in the center of the ONC might affect the oscillation, but based on the star to gas mass ratios in the region, this effect is not dominant. The gas filament, both its gravitational-magnetic oscillations and the gravitational tides that it generates, naturally explain all three of the above elements.

The first key point is tides represent the differential acceleration on a particle relative to the center of mass of a system that is moving through an external potential. If the cluster were sitting in a non-accelerating external potential, there would be no tides: the particles (stars) would simply reorganize themselves according to the external potential and their own velocity dispersion (somewhat modified by their self-potential, which is subdominant). On the other hand, if the gas filament is accelerating due to non-gravitational (i.e., magnetic) forces, then the cluster (which is only subject to gravitational forces) will always be moving relative to the gas and so will be subject to tides. In this way, the filament potential sets the structural parameters of the ONC. These tides will then automatically suppress low density structures, such as the outskirts of the cluster (for spherical analogs see [Lamers et al. 2005](#); [Gieles & Renaud 2016](#); [Renaud et al. 2011](#)).

As shown by [Stutz & Gould \(2016\)](#), the stars are born (as protostars) on the filament and have essentially zero velocity relative to the filament. That is, the specific kinetic energy of the protostars is ~ 6 times smaller than that of the stars. On the other hand, the stellar velocity dispersion is comparable to the velocity amplitude of filament oscillations, which is one of the pieces of evidence that led [Stutz & Gould \(2016\)](#) to conclude that the stars were being ejected from the filament as they mechanically decoupled from the gas. This ejection mechanism naturally explains why the cluster has a core: the core is populated by stars that have been ejected (and fall into the potential well of the cluster) over a range of velocities and positions as the filament oscillates. Moreover, this naturally explains why the crossing time of the stars is similar to that of the filament oscillations.

Next, we should ask why there is a cluster at all if the kinematics and potential are dominated by the filament? The cluster forms first of all because of a whip-like action of the oscillating filament, which induces a shock, and consequent rapid concentration of gas, near the filament's termination point at any given time. NGC 1981 ([Pillitteri et al. 2013](#)) was formed at the end of the Orion A filament in this way during one such whip-like snap about 4 Myr ago, and NGC 1977 ([Peterson & Megeath 2008](#)) was formed in the next whip-like snap about 2 Myr ago. Each of these cluster formation episodes truncated the Orion A filament progressively further to the south. These are the only two such episodes that are recognizable from the fossil record, but undoubtedly there were earlier ones that occurred as Orion A gradually retracted itself from Orion B further to the north. The ONC is the result of the third, and currently ongoing, such snap that we can recognize. Further evidence that the ONC is the product of a whip-like snap is provided by the N_2H^+ map of [Hacar et al. \(2017\)](#); see also [Tatematsu et al.](#)

(2008). This shows that the high-density gas is not simply concentrating to form stars, but is also breaking into pieces just ~ 0.5 pc to the south of the star cluster. These data also show that the dense gas is converging about ~ 0.25 pc to the south of the center of the cluster, and thus far outside the gravitational center of the cluster, which may be further evidence that the gas velocities reflect larger-scale filament dynamics rather than infall into the star cluster.

However, while the cluster does not dominate the gravitational field in the direction perpendicular to the filament at any radius (see [Fig. 10](#)), it provides most of the restoring force in the direction parallel to the filament. We say “most” because the filament is actually denser in the neighborhood of the cluster than in other parts of the ISF, and so does provide some restoring force in this direction.

Hence, in this picture, the gas continuously pours into the “snapping point” of the filament, which is determined by its global structure, including oscillations. The conversion of gas into stars (acting as “sink particles”, e.g., [Bate et al. 1995](#)) reduces the local pressure, which drives a continuous replacement by new gas. Because the stars are born along the filament, and are confined by the gas potential along the directions transverse to the filament, their self-gravity can build up to the point that it restricts their dispersal along the filament.

How does the gas filament cut off growth of the cluster core just at the point that the cluster's gravity is beginning to dominate? Again, the key lies in the filament's oscillations. As long as the nascent proto-cluster remains a basically passive accumulation of stars, its collective impact on the filament likewise remains minimal. But to the extent that the cluster becomes self-gravitating and capable of following its own inertial orbit, it begins to impact the gas flows within the filament as the filament oscillates away from it. Indeed, there is some evidence from the extinction measurements (e.g., [O'dell 2001](#); [Wen & O'dell 1995](#)) that the cluster center is currently displaced from (somewhat in front of) the gas filament.

This picture gives insight not just into the past history of the ONC, but also its future. Just as individual protostars separate from the filament at the moment when their self-gravity enables them to marginally decouple mechanically from the gas, so the ONC proto-cluster as a whole will separate from the filament as it becomes marginally self-gravitating and can decouple gravitationally from the filament. In the case of the individual protostars, their exit from the filament initiates the next phase of their evolution as disk-bearing stars that have been cut off from external gas accretion. The proto-cluster's exit likewise initiates a new phase of life as a nascent cluster that is cut off from the aggregation of new stars.

In a richer environment than Orion, perhaps several such marginally bound nascent clusters would merge to form a truly self-gravitating system. This will not be the fate of the ONC, however. Rather, because it will exit the filament when it is only marginally self-gravitating, it will lose a large fraction of its stars and become a shadow of its former self, similar to NGC 1977 and NGC 1981. In the still more distant future, less than 10 Myr, the ONC will likely completely disperse, similar to the fate of the clusters that formed before NGC 1981 as the gap opened up between the Orion A and Orion B filaments.

Future numerical simulations coupling oscillating filaments to N-body dynamics (Boekholt et al. 2017, Matus Carrillo et al., in prep.) of star clusters will stringently test this hypothesis. Furthermore, ALMA observations of the number and distribution of protostars within the ONC will provide essential observational constraints on the origin of the stars populating the cluster.

6 ACKNOWLEDGMENTS

We thank the referee for their helpful comments which aided in the clarity of the presentation. We thank Andrew P. Gould, Tjarda C. N. Boekholt, Dominik R. G. Schleicher, Michael Fellhauer, Xiaoling Pang, and S. Thomas Megeath for many stimulating discussions. We are very grateful to S. Thomas Megeath for providing the *Spitzer* star count data in map form. We are grateful for the generous hospitality of Shanghai Normal University (SNU) where a portion of this work was carried out. We acknowledge funding from the "Concurso Proyectos Internacionales de Investigación, Convocatoria 2015" (project code PII20150171) and the BASAL Centro de Astrofísica y Tecnologías Afines (CATA) PFB-06/2007. This paper includes data from *Herschel*, a European Space Agency (ESA) space observatory with science instruments provided by European-led consortia and with important participation from NASA. We include data from the Atacama Pathfinder Experiment (APEX), a collaboration between the Max-Planck-Institut für Radioastronomie, the European Southern Observatory, and the Onsala Space Observatory.

REFERENCES

Bally J., Langer W. D., Stark A. A., Wilson R. W., 1987, *ApJ*, **312**, L45
 Bate M. R., 2009, *MNRAS*, **392**, 590
 Bate M. R., Bonnell I. A., Price N. M., 1995, *MNRAS*, **277**, 362
 Bianchini P., Sills A., Miholics M., 2017, *MNRAS*, **471**, 1181
 Binney J., Tremaine S., 2008, *Galactic Dynamics: Second Edition*. Princeton University Press
 Boekholt T. C. N., Stutz A. M., Fellhauer M., Schleicher D. R. G., Matus Carrillo D. R., 2017, preprint, ([arXiv:1704.00720](https://arxiv.org/abs/1704.00720))
 Da Rio N., Robberto M., Hillenbrand L. A., Henning T., Stassun K. G., 2012, *ApJ*, **748**, 14
 Da Rio N., Tan J. C., Jaehnig K., 2014, *ApJ*, **795**, 55
 Da Rio N., et al., 2016, *ApJ*, **818**, 59
 Feigelson E. D., et al., 2005, *ApJS*, **160**, 379
 Fujii M. S., Portegies Zwart S., 2016, *ApJ*, **817**, 4
 Getman K. V., et al., 2014, *ApJ*, **787**, 108
 Gieles M., Renaud F., 2016, *MNRAS*, **463**, L103
 Gutermuth R. A., Megeath S. T., Pipher J. L., Williams J. P., Allen L. E., Myers P. C., Raines S. N., 2005, *ApJ*, **632**, 397
 Gutermuth R. A., Megeath S. T., Myers P. C., Allen L. E., Pipher J. L., Fazio G. G., 2009, *ApJS*, **184**, 18
 Hacar A., Alves J., Tafalla M., Goicoechea J. R., 2017, preprint, ([arXiv:1703.03464](https://arxiv.org/abs/1703.03464))
 Hartmann L., Burkert A., 2007, *ApJ*, **654**, 988
 Hillenbrand L. A., Hartmann L. W., 1998, *ApJ*, **492**, 540
 Jones B. F., Walker M. F., 1988, *AJ*, **95**, 1755
 Kainulainen J., Stutz A. M., Stanke T., Abreu-Vicente J., Beuther H., Henning T., Johnston K. G., Megeath T., 2016, preprint, ([arXiv:1603.05688](https://arxiv.org/abs/1603.05688))
 Kounkel M., et al., 2017, *ApJ*, **834**, 142

Kroupa P., 2000, *New Astron.*, **4**, 615
 Kroupa P., Petr M. G., McCaughrean M. J., 1999, *New Astron.*, **4**, 495
 Kroupa P., Aarseth S., Hurley J., 2001, *MNRAS*, **321**, 699
 Lamers H. J. G. L. M., Gieles M., Bastian N., Baumgardt H., Kharchenko N. V., Portegies Zwart S., 2005, *A&A*, **441**, 117
 Megeath S. T., et al., 2012, *AJ*, **144**, 192
 Megeath S. T., et al., 2016, *AJ*, **151**, 5
 Meingast S., et al., 2016, *A&A*, **587**, A153
 Menten K. M., Reid M. J., Forbrich J., Brunthaler A., 2007, *A&A*, **474**, 515
 O'dell C. R., 2001, *ARA&A*, **39**, 99
 Peterson D. E., Megeath S. T., 2008, *The Orion Molecular Cloud 2/3 and NGC 1977 Regions*. p. 590
 Pillitteri I., et al., 2013, *ApJ*, **768**, 99
 Plummer H. C., 1911, *MNRAS*, **71**, 460
 Portegies Zwart S. F., 2016, *MNRAS*, **457**, 313
 Portegies Zwart S. F., McMillan S. L. W., Gieles M., 2010, *ARA&A*, **48**, 431
 Renaud F., Gieles M., Boily C. M., 2011, *MNRAS*, **418**, 759
 Sandstrom K. M., Peek J. E. G., Bower G. C., Bolatto A. D., Plambeck R. L., 2007, *ApJ*, **667**, 1161
 Schlafly E. F., et al., 2014, *ApJ*, **786**, 29
 Schleicher D. R. G., Stutz A. M., 2017, preprint, ([arXiv:1705.06302](https://arxiv.org/abs/1705.06302))
 Stanke T., et al., 2010, *A&A*, **518**, L94
 Stutz A. M., Gould A., 2016, *A&A*, **590**, A2
 Stutz A. M., Kainulainen J., 2015, *A&A*, **577**, L6
 Stutz A. M., et al., 2013, *ApJ*, **767**, 36
 Tatematsu K., Kandori R., Umemoto T., Sekimoto Y., 2008, *PASJ*, **60**, 407
 Tobin J. J., Hartmann L., Furesz G., Mateo M., Megeath S. T., 2009, *ApJ*, **697**, 1103
 Wen Z., O'dell C. R., 1995, *ApJ*, **438**, 784

APPENDIX A: FROM AN M/L TO A VOLUME DENSITY

We assume polytrope density and projected density profiles of the form

$$\rho(r) \equiv K(1 + (r/a)^2)^{-\gamma}; \quad \Sigma(b) \equiv C(1 + (b/a)^2)^{-\beta}.$$

Here,

$$\begin{aligned} \Sigma(b) &= \int_{-\infty}^{\infty} dz \rho(\sqrt{z^2 + b^2}) = 2 \int_0^{\infty} dz K((a^2 + b^2)/a^2 + z^2/a^2)^{-\gamma} \\ &= 2(1 + (b/a)^2)^{-\gamma} \int_0^{\infty} dz K(1 + z^2/(a^2 + b^2))^{-\gamma} \\ &= 2(1 + (b/a)^2)^{-\gamma} \sqrt{a^2 + b^2} \int_0^{\infty} \frac{dz}{\sqrt{a^2 + b^2}} K(1 + z^2/(a^2 + b^2))^{-\gamma} \\ &= 2K(1 + (b/a)^2)^{-\gamma + 0.5} a \int_0^{\infty} dx (1 + x^2)^{-\gamma}. \end{aligned}$$

So, $\beta = \gamma - 0.5$ and $C = 2Ka \int_0^{\infty} dx (1 + x^2)^{-\gamma}$ where

$$\begin{aligned} \int_0^{\infty} dx (1 + x^2)^{-\gamma} &= \int_0^{\pi/2} d\theta \cos^{2\gamma-2} \theta \\ &= 0.5(-1/2)!(\gamma - 3/2)!/(\gamma - 1)! \end{aligned}$$

which for $\gamma = 5/2$ is $0.5(-1/2)!/(3/2)! = 2/3$. That is, $C = (4/3)aK$.

Now consider an “orange slice”, of infinitesimal width, but offset from the center by q :

$$\lambda(q) = \int_{-\infty}^{\infty} dy \Sigma(\sqrt{q^2 + y^2}) = 2 \int_0^{\infty} dy C((q^2 + a^2 + y^2)/a^2)^{-\beta}$$

Then, using exactly the same algebraic steps as above

$$\lambda(q) = \kappa(1 + (q/a)^2)^{-\delta}$$

where $\delta = \beta - 0.5$ and $\kappa = Ca(-1/2)!(\beta - 3/2)!/(\beta - 1)!$

Finally, the total mass in a thick slice within $\pm L/2$ of the center is

$$\begin{aligned} M_{\text{slice}} &= \int_{-L/2}^{L/2} dq \kappa(1 + (q/a)^2)^{-\delta} = 2\kappa a \int_0^{L/2} \frac{dq}{a} \kappa(1 + (q/a)^2)^{-\delta} \\ &= 2\kappa a \int_0^{L/2a} dx (1 + x^2)^{-\delta} = 2\kappa a \int_0^{\tan^{-1}(L/2a)} d\theta \cos^{2\delta-2} \theta \\ &= 2Ka^3 \frac{[(-1/2)!]^2 (\gamma - 3/2)! (\beta - 3/2)!}{(\gamma - 1)! (\beta - 1)!} \int_0^{\tan^{-1}(L/2a)} d\theta \cos^{2\delta-2} \theta \\ &= 2Ka^3 \frac{[(-1/2)!]^2 (\beta - 1)! (\beta - 3/2)!}{(\beta - 1/2)! (\beta - 1)!} \int_0^{\tan^{-1}(L/2a)} d\theta \cos^{2\delta-2} \theta \\ &= \frac{2\pi Ka^3}{\delta} \int_0^{\tan^{-1}(L/2a)} d\theta \cos^{2\delta-2} \theta \end{aligned}$$

This can be evaluated numerically, but for the special case of $2\delta = \text{integer}$, it can be done analytically. In particular, for $\gamma = 5/2$, i.e., $\delta = 3/2$, we obtain

$$\int_0^{\tan^{-1}(L/2a)} d\theta \cos^{2\delta-2} \theta = \sin(\tan^{-1}(L/2a)) = \frac{1}{\sqrt{1 + (2a/L)^2}}.$$

That is,

$$M_{\text{slice}} = \frac{4\pi Ka^3}{3} \frac{1}{\sqrt{1 + (2a/L)^2}}.$$

Note that for the special case of $L = \infty$, we recover the standard formula for the cluster mass. For the special case of a thin slice (which was previously considered) we get $M_{\text{slice}} = 2\pi Ka^2 L/3$, i.e., proportional to L . Motivated by this “ M/L ” form, we can write the general case as

$$M_{\text{slice}} = \frac{2\pi Ka^2 L}{3} \frac{1}{\sqrt{1 + (L/2a)^2}}. \quad (\text{A1})$$

From this, we can see that for the particular case of $(L, a) = (0.5, 0.36)$ pc, the “adjustment factor” relative to the previous “thin slice” reasoning is $1/\sqrt{1 + (0.5/0.72)^2} = 0.82$.

The net result is that for our parameters, $\beta = 2.0$, $a = 0.36$ pc, $L = 0.5$ pc,

$$K = \frac{3}{2\pi a^2} \frac{M_{\text{slice}}}{L} \sqrt{1 + (L/2a)^2} = \frac{4.48}{\text{pc}^2} \frac{M_{\text{slice}}}{L}.$$

This paper has been typeset from a $\text{\TeX}/\text{\LaTeX}$ file prepared by the author.

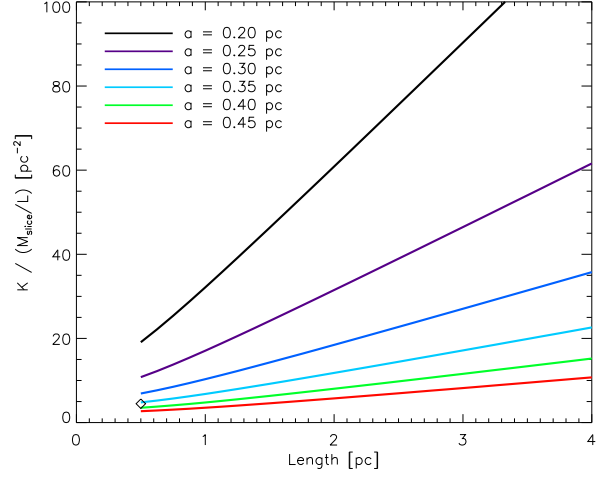


Figure A1. Relationship between slice thickness (L), Plummer profile softening scale (a), total mass per unit length (M_{slice}/L), and the normalization of the Plummer density profile shown in equation A1. The diamond symbol indicates the particular case for the ONC.